1 **Patient-derived glioblastoma cells (GBM) exhibit distinct biomechanical profiles associated**

2 **with altered activity in the cytoskeleton regulatory pathway.**

3

4

5 Amelia Foss[a], Michele Zanoni[b], Woong Young So[a], Lisa Jenkins[a], Luigino Tosatto[c], Daniela

6 Bartolini[d], Michael M Gottesman[a], Anna Tesei[b] *, Kandice Tanner [a]*

7

8

9

10

11

12 [a]Laboratory of Cell Biology, Center for Cancer Research, National Cancer Institute, National

13 Institutes of Health

14 [b]Biosciences Laboratory, Istituto Scientifico Romagnolo per lo Studio e la Cura dei Tumori

15 (IRST), IRCCS, Meldola, Italy

16 [c]Department of Neurosurgery, AUSL Romagna, M.Bufalini Hospital, Cesena, Italy

17 [d]Department of Human Pathology, AUSL Romagna, M.Bufalini Hospital, Cesena, Italy

18

19 * Corresponding author information:

20 Dr. Kandice Tanner; Center for Cancer Research, National Cancer Institute, Building 37, Room

21 2132, Bethesda, MD 20892; Ph: 260-760-6882; Email: kandice.tanner@nih.gov

22 Dr. Anna Tesei Biosciences Laboratory, Istituto Scientifico Romagnolo per lo Studio e la Cura dei

23 Tumori (IRST), IRCCS, Meldola, Italy; Email: anna.tesei@irst.emr.it

24

ABSTRACT

Glioblastoma multiforme (GBM) is the most commonly diagnosed brain cancer in adults, characterized by rapid proliferation and aggressive invasion into the stroma. Advances in our understanding of the molecular subtypes of GBM have provided attractive druggable targets. However, the high degree of heterogeneity both among patients and within individual tumors has proven a significant challenge for the development of effective therapies. We hypothesized that this heterogeneity is also represented in the mechanical phenotypes of GBM, as the physical properties of tumor tissue strongly influence elements of tumor progression including cell cycle regulation, migration, and therapeutic resistance. To assess these phenotypes, we employed optical trap-based active microrheology to determine the viscoelastic properties of patient-derived GBM cells in 3D hydrogels mimicking the brain ECM. We found that each GBM cell line had a distinct rheological profile as a function of treatment status, and cell lines could be further characterized by strong power law dependence describing intracellular viscoelastic behavior. Single-cell phenotyping according to power law dependence was able to identify subpopulations of cells within the treatment-resistant line. Finally, proteomic analysis indicated that altered mechanical profiles were associated with differential cytoskeletal regulation, particularly in actin- and myosin-binding pathways. This work suggests that evaluating mechanical properties may serve as a valuable strategy for the further stratification of these tumors, and encourages the investigation of cytoskeleton regulation as a potential therapeutic target for GBM.

Introduction

Glioblastoma multiforme (GBM) is the most lethal cancer of the central nervous system, and most patients succumb to the disease within 1-2 years after diagnosis[1]. Transcriptomic and histopathological analysis have determined that GBM tumors adopt a multitude of phenotypic, cellular, genetic, and epigenetic subtypes[2, 3]. These molecular sub-types are characterized by amplification, absence, or mutation of genes that encode for growth factor receptors, metabolic regulators, and known tumor suppressors[2, 3]. This wealth of molecular data provides attractive and actionable biomarkers. However, clinical trials based on this stratification have not yielded curative treatment[1]. Moreover, recent data have shown that these sub-types are plastic, as an interconversion of distinct states is observed during tumor evolution[3]. It is thought that treatment efficacy is obfuscated due to the multifactorial diversity found intratumorally and across patients. Thus, further stratification of "multiformes" may be needed to develop effective therapeutic interventions.

GBM plasticity may in part be due to specific components of the brain microenvironment[4-7]. The physical properties of the brain microenvironment have been shown to influence drug response and tumor growth[4, 8, 9]. In addition, motile GBM cells can remodel the surrounding matrix, which, in turn, increases motility[4, 8-11]. This dynamic coupling between cell and environment also changes the phenotype of the cells themselves[11, 12]. The combined viscous and solid behavior that defines the single cell mechanical phenotype may also be a viable target to assess phenotypic plasticity. This mechano-phenotype regulates the kinetics and diversity of enzymatic processes which in turn drive cell fate[13-15]. Subcellular components such as the cytoskeleton, nucleus and a copious distribution of cytoplasmic proteins, enzymes and solutes drive the viscoelastic behavior of single cells[13-17]. Thus, defining these mechanical states may

67   offer additional insight in what may drive the interchange between sub types in GBM. However,

68   it is not known if single cells adopt distinct mechanical phenotypes as a function of subtype or

69   within a given subtype for patient derived GBM cells.

70   Real-time mechanical mapping of GBM tumors in patients has been achieved using

71   modalities based on magnetic resonance[18-20]. Using single and multi-frequency magnetic

72   resonance elastography, correlations between mechanical properties and tumor grade and

73   mutational status have been reported[21]. The technique has also been successful in resolving the

74   relative importance of the fluidity for distinct brain tumors[18]. Intratumoral heterogeneity can be

75   distinguished for regions corresponding to ~100s of cells. However, single cell resolution has not

76   been demonstrated at this time *in vivo*. One strategy to address this knowledge gap would be a

77   combined approach where one employs the use of biomimetic platforms that mimic the *in vivo*

78   GBM microenvironment with that of single cell rheological modalities such as brillouin

79   microscopy, and optical and magnetic tweezers. Using optical tweezer based active

80   microrheology, we have previously shown that we can map the mechanical coupling of tumor

81   cells embedded in distinct 3D extracellular matrix (ECM) hydrogels[16]. Here, we aimed to

82   determine if patient derived GBM cells display heterogeneities in their mechanical phenotype

83   similar to the molecular heterogeneity observed in patients.

84   We reasoned that the intratumor heterogeneity in clinical presentation and genetic

85   characteristics also includes heterogeneity in mechanical phenotype and cytoskeletal dynamics,

86   which may contribute to differing tumor progression and altered invasion profiles. To investigate

87   this question, we embedded patient-derived GBM cells into 3D hyaluronic acid-based hydrogels

88   to mimic the extracellular matrix environment of the brain. We determined that among three

89   patient-derived GBM cell lines and a model cell line, each line had a distinct viscoelastic profile

90   indicating cell stiffness and hysteresivity, or how liquid- or solid-like a substance behaves.

91   Moreover, we determined that within each cell line, a range of mechanical phenotypes is observed.

92   However, classification of cells based on power law dependence revealed that a cell line obtained

93   from a relapsed patient stratified into two distinct populations, whereas the treatment naïve cell

94   lines showed single populations with varying widths of distribution. Immunofluorescence shows

95   altered patterns of actin cytoskeletal organization among lines. Supporting these data, cytoskeletal

96   regulation pathways, including cytoskeletal protein-binding and myosin-binding pathways are

97   significantly altered among cell lines according to mass spectrometry analysis. Specifically,

98   Myosin IIC, associated with cytoskeleton dynamics, cell adhesion, and tumor cell invasion, is

99   differentially abundant among lines, and serves as a promising target for further investigation.

100

101

102

103

104 **Results**

105 **Mapping the intracellular heterogeneity of a single cell in 3D hyaluronic acid**

106   In optical trap (OT)-based rheology, local piconewton forces are applied to objects such as

107 beads and organelles [22-24]. From the induced displacement of these objects, determination of

108 the underlying local physical properties of the material can be achieved, with the caveat that the

109 mesh size of the material is smaller than the probe. Thus, we first asked if we can map cytoplasmic

110 heterogeneity using 1 μm-diameter polystyrene beads as local sensors. To address this question,

111 we employed a biomimetic model of the brain ECM microenvironment using the immortalized

112 U87 GBM cell line. Cells were harvested and incubated in media supplemented with 1 μm-

113 diameter polystyrene beads. These cells were embedded in 3D hyaluronic acid hydrogels at

114 densities that minimized nearest neighbor effects and ensured cells saw an isotropic distribution

115 of matrix (Figure 1A). OT-based active microrheology was performed on intracellular beads with

116 a total amplitude of oscillation of 200 nm (20nm per frequency (ω)) at a power of 200mW at the

117 back aperture over a range of frequencies spanning 7-15 kHz (Figure 1B). Using vis a vis

118 calibration and FDT, we quantitated the complex modulus, G* for each bead. $G^* = |G^*|\exp(i\delta) =$

119 G' + iG'', can be then broken down into magnitude $|G^*| = (G'^2 + G''^2)^{1/2}$, in which G' represents

120 the storage modulus and G'' represents the loss modulus. We also assessed crossover frequency

121 the two components, which indicates when the material properties transition from solid-like to

122 liquid-like. We determined the local physical properties for three to five intracellular beads

123 randomly distributed in the cytoplasm of individual cells (Figure 1C). We found that, for a given

124 cell, the values of G' and G'' for each bead varied from 6 Pa - 2 kPa for ω ranging from 7-15kHz.

125 For each bead, we observed a strong power law dependence for frequencies greater than 400Hz

126 (HF) compared to a relatively shallow curve at frequencies below 400Hz (LF).

127   We then quantified the average mechanical properties for a given population of cells. First, the

128   phenotype, G', G", of each cell was determined by averaging measurements for each bead within

129   a given cell (Figure 1D). We then averaged the values for thirty cells. We observed G' vs G" values

130   of 18.8 - 602.5 Pa. and a crossover frequency at $\omega = 2.73$ kHz. The distinct strong power law

131   dependence following G', G" $\sim A(\omega)^b$ at $\omega > 400$Hz (HF) and shallow slope for frequencies below

132   400Hz (LF) is maintained for an ensemble population of cells (Figure 1D).

133   **Patient derived GBM samples show distinct mechanical properties as a function of treatment**

134   **status**

135   We next examined the rheological properties of primary GBM cells. We chose three

136   distinct cell lines: two that were treatment naïve and one that was derived from a relapsed tumor

137   following radiation and chemotherapy (Figure 2A). We confirmed that the intracellular

138   heterogeneity observed in the immortalized cell line was also present in primary cells

139   (Supplemental Figure 1A-C). For each primary cell line, the mechanical phenotype is dominated

140   by the elastic modulus where the crossover frequency ranged from 2.5-4kHz (Figure 2B). As

141   observed with the immortalized cell line, values of G' and G" obeyed a power law at high

142   frequencies in the primary lines. For the treatment naïve cell lines the value of exponent b ranged

143   from 0.231-0.259 for G' and from 0.685-0.712 for G". Similarly, for the treatment resistant line,

144   G' followed a weaker power law dependence with a value of 0.268 for the exponent b, and a

145   stronger dependence for G" where the value of the exponent b is 0.688. The treatment-resistant

146   line showed a markedly higher $\omega_{crossover}$ at 4.06 kHz compared to the lower crossover frequencies

147   of treatment-naïve lines ($\omega_{crossover} = 2.94$ kHz, 2.95 kHz for GB40 and GB70, respectively) (Figure

148   2B, Supplemental Figure 2B). We can then transform these data into plots of complex moduli.

149   These plots show that the absolute value of G* is dominated by the storage modulus whereas the

150   component from the loss modulus dominated the exponent of the power law dependence (Figure

151   2C). To assess relative stiffnesses, we compared the Log_2 ratios of $G^*(\omega)$ for each cell line. From

152   this analysis, one naïve cell line (GB70) was stiffer than the primary and immortalized cell lines

153   (GB34 and GB40, and U87, respectively) (Figure 2D). The immortalized cell line showed a similar

154   stiffness compared to treatment resistant cell line at high frequencies. As predicted, at the higher

155   frequencies, G^* showed a stronger power law dependence where slopes ranged from 0.47 to 0.56

156   (Figure 2C)[25]. To assign a mechanical phenotype to each of the cell lines, we examined the

157   power law dependence of $G^* \propto A\omega^b$ for each population, where materials that behave like semi-

158   flexible polymers follow b=0.75, with b=0.5 indicative of flexible polymers. We determined that

159   treatment resistant cells behaved relatively more like flexible polymers compared to treatment

160   naïve cells, with a b=0.47 for the GB34 line compared to b = 0.48 and b = 0.49 for GB40 and

161   GB70 lines, respectively.

162   **Single cell phenotyping using power law dependence identifies sub-populations in treatment**

163   **resistant GBM cells.**

164   GBM tumors are comprised of cells that show a diversity of phenotypes hence the use of

165   "multiforme" in its tumor classification[1, 3]. Thus, we revisited our individual cell measurements

166   to understand the distribution of the mechanical phenotypes. Among all cell lines, the individual

167   cell measurements ranged from ~10 - 2500Pa for the full spectrum of frequencies, displaying

168   significant heterogeneity within each line (Figure 3A). Having observed a robust power law at

169   higher frequencies, we then calculated the individual exponents on a single cell basis (Figure 3B).

170   We observed that the treatment resistant GB34 cells segregate into two populations, cells that

171   behave like flexible and semi-flexible polymers. In contrast, the treatment naive cell lines show

172   single populations, one (GB40) that can be classified with phenotypes akin to flexible polymers

173   whereas another cell line (GB70) showed a broad distribution of states. In contrast, phenotypes of

174   the immortalized cell line, U87 clustered more closely with phenotypes akin to semi-flexible

175   polymers. We also observed these population dynamics in single cell analysis of intracellular

176   hysteresivity, as resistant GB34 cells appear to segregate into two populations, GB70 cells show a

177   broad distribution of characteristics, and the remaining treatment naïve lines cluster close together

178   (Supplemental Figure 2A).

179   **GBM lines show distinct patterns of cytoskeletal organization.**

180   Mechanical phenotypes can be modulated by many factors such as treatment and culture

181   conditions (i.e. primary vs immortalized). Thus, to assess what molecular mechanisms may

182   regulate the differences in mechanical phenotypes, we focused on two of the treatment naïve cell

183   lines. Differential analysis of the proteome revealed that Myosin IIB (MYH10) and IIC (MYH14)

184   were upregulated in the GB40 cell line compared to the more heterogenous GB70 line (Figure 4A-

185   B). Myosin IIB and IIC have been implicated as regulators of actin organization [26, 27]. In cells,

186   actin-dependent regulation of cytoskeletal architecture provides a significant contribution to single

187   cell mechanical properties. Thus, we assessed actin structures using immunostaining (Figure 4C).

188   In the cell line that showed a narrow distribution akin to flexible polymers, we observed actin

189   structures assembled into multi-foci within the cytoplasm with minimal cortical staining. However,

190   in the second cell line that showed broad distribution of mechanical states, two distinct of actin

191   structures and distributions were observed: 1) multi foci and 2) diffuse with strong cortical

192   staining. Shape analysis of these cell lines also showed a difference in circularity, where GB40

193   cells with stronger punctate staining were less spherical than the GB70 cells (Supplemental Figure

194   3). Furthermore, pathway analysis indicates significant upregulation of cytoskeletal organization

195   functions in the GB40 line, including actin and myosin binding (Figure 4D).

Discussion

In spite of our knowledge of molecular sub-types of GBM, curable treatment remains elusive[1]. Treatments include chemotherapy (temozolomide), radiation, and surgical resection, and occur only if these interventions do not impair cognition and quality of life [1, 28]. Phenotypic plasticity and microenvironmental elements are potent factors affecting drug sensitivity and efficacy [1, 3]. These factors are further complicated by intratumor and intertumoral heterogeneities in patients, which have thus far been challenging to model at high resolution [1-3, 7, 29]. Our lab has previously measured the microscale mechanical coupling of tumor cells with that of a 3D biomimetic hydrogel [16]. Here, in an effort to understand mechanical heterogeneity in glioblastoma, we employed optical trap based active microrheology to characterize single cell mechanical phenotypes of patient derived primary GBM cells in a 3D brain mimicking matrix. We measured the single cell mechanophenotype of three patient-derived GBM primary cell lines and an immortalized cell line. Each of these had a distinct viscoelastic profile indicating cell stiffness and hysteresivity, or how liquid- or solid-like a substance behaves. Examination of power law dependence at higher frequencies revealed that the treatment resistant GBM cells can be grouped into two distinct populations, while most of the treatment naïve cell lines were centered on a single population and the other showed a broad distribution of states. For this cell line we determined that these cells adopted multiple states with different patterns of actin cytoskeletal organization.

The mapping of cellular mechanics has been achieved using multiple modalities including optical and magnetic tweezer based active rheology, passive rheology, atomic force microscopy and Brillouin microscopy[17, 30, 31]. Measurements of single cells in suspension can be performed using an optical stretcher and the high throughput, RT-DC system[32]. Previously, intracellular measurements obtained for yeast cells and normal mammalian cells ranging from

219   neurons and fibroblasts to breast epithelial cells have been achieved using AFM and Brillouin

220   microscopy [33-35]. These values ranged from ~0.5-2kPa for Young's modulus and a calibrated

221   longitudinal modulus respectively for a relatively narrow frequency range and non-overlapping

222   regime[33-35], and interestingly, single cell measurements revealed a difference in mechanical

223   properties due to differentiation status in fetal neural progenitor cells[14]. Here, we determined

224   that the GBM cells are comparatively softer, where the measured complex moduli ranged from

225   0.02-1kPa across our multiplexed 20 frequencies. This is in line with previous measurements using

226   OT based microrheology of 2 micron beads in breast cancer cells in cultured on 2D micropatterned

227   substrates and 1 micron beads of breast cancer cells cultured in 3D hydrogels[16, 36]. Moreover,

228   our cells showed differences in stiffnesses due to treatment status, where treatment naïve cells

229   were softer than the treatment resistant. This result is consistent with changes of mechanical

230   phenotypes due to cell fates observed in comparison of differentiation status and drug

231   resistance[14, 33]. This discrepancy between the OT measurements and the non-probe-based

232   techniques can be due to four factors. First, mechanical phenotype is strongly dependent on the

233   length and temporal scales of the technique. Second, mechanical properties obtained using probe-

234   based techniques such as OT/MT and particle based passive rheology are highly dependent on

235   probe size. Third, healthy, normally-programed cells are often "stiffer" than their cancerous

236   counterparts. Last, mechanical properties are dependent on culture conditions, such as adherent or

237   suspended culture, and dimension (2D vs 3D)[9, 37-39].

238   Access to broad frequencies allowed us to examine a dynamic range of complex behaviors.

239   Our measurements compare well with previous measurements, where G* is characterized by a low

240   frequency elastic plateau regime and a high frequency liquid-like regime characterized by power-

241   law frequency dependence[25, 38, 40]. In particular, actin cytoskeleton dynamics dominate the

242   mechanical response due to the size of the probe used in these experiments. At higher frequencies

243   (>400Hz), the exponent from the formulaic power dependence is equal to 1 for purely viscous

244   response. If contributions due to the cytoskeleton are the largest contributors, then these values are

245   0.5, 0.75 and 0.875 for transverse and longitudinal modes of relaxation respectively [41]. We

246   previously demonstrated that this exponent can vary from 0.2-0.8 for breast cells cultured in 3D

247   hydrogels based on the chemistry of the hydrogel and perturbation of the cytoskeleton [16]. Similar

248   examination was performed for cells cultured in 2D using high frequency AFM[40]. In these

249   measurements, a double exponential fit was used for the elastic and liquid like regime. This value

250   ranged from 0.15- 0.9 based on cell type and pharmacological inhibition of actin. In a similar

251   comparison, an exponent of 0.41 was calculated for a breast cancer cell line[42]. Here, our

252   measurements showed a range from 0.47-0.56.

253   We used this exponent to categorize the single cells in an effort to describe a

254   complementary mechanical phenotype reminiscent of the molecular phenotypic classification used

255   for GBM. In this work, we observed a difference due to treatment status. It remains to be seen,

256   however, if the mechanical phenotype can be linked to mutation status as observed for MRE

257   measurements[21]. Instead our data hint at the importance of factors that direct cellular mechanics,

258   such as the actomyosin pathway, as potential regulators of the "multiformes" within the GBM

259   population.

260   Non-muscle myosin proteins have been implicated in tumor proliferation and invasion.

261   Briefly, decreased activity of Myosin IIA and IIB in GBM cells, particularly Myosin IIA, resulted

262   in reduced tumor cell invasion *in vitro* and in a rodent model [43-45]. However, decreased Myosin

263   IIA expression also enhanced proliferation in a manner dependent on the mechanical properties of

264   the tissue microenvironment[45]. Our data, obtained using direct comparison of the proteome of

265   two representative treatment naïve cell lines, also revealed differential expression of cytoskeletal

266   regulation pathways, including cytoskeletal protein-binding and myosin-binding pathways.

267   Specifically, Myosin IIC, associated with cytoskeleton dynamics, cell adhesion, and tumor cell

268   invasion within brain ECM, was differentially abundant among lines [26, 27, 46]. Our data

269   presents additional evidence that these myosin isoforms may be key factors in GBM and serve as

270   promising targets for further investigation.

271

272   **ACKNOWLEDGEMENTS**

275

276

277

278

279

280

281

282

283

284

285

286

287

288 **Methods**

289 **Patient-derived glioblastoma cells**

290 Primary human glioblastoma cells were obtained directly from patient tumor specimens processed

291 within 2 hours of surgery, as previously described[47]. Briefly, adult GBM tissues obtained from

292 patients underwent surgical resection and sampled by a pathologist were dissected and digested in

293 an enzyme mix solution. Patient-derived GBM cells were plated in NeuroCult NS-A serum-free

294 medium (StemCell Technologies, Vancouver, BC, Canada) supplemented with 20 ng/ml of

295 epidermal- and 10 ng/ml of fibroblast-growth factor (Sigma-Aldrich), 1% penicillin/streptomycin

296 (GE Healthcare, Milan, Italy) and 2% amphotericin B (Euroclone) and maintained under hypoxic

297 conditions (1% O2) in a humidified 37 °C, 5% CO2 incubator. All the primary GBM cell lines

298 were checked periodically for mycoplasma contamination using the MycoAlertTM Mycoplasma

299 Detection Kit (Lonza, Basel, Switzerland). All Patient-derived biological samples were collected

300 according to a protocol approved by Italian Local Ethics Committee (CE IRST IRCCS-AVR,

301 protocol 2439/2018) and all the patients enrolled have signed an informed consent for the genetic

302 analyses and for the use of the results for research purposes.

303 **Cell Culture**

304 U87 cells were grown and maintained as previously described at 37ºC in normoxic conditions

305 (20% O_2, 5% CO_2) in Dulbecco's Modified Eagle Medium (DMEM, 10% FBS, 1%

306 Penicillin/Streptomycin, 1% L-glutamate)[48]. Patient-derived glioblastoma (GBM) cells (GB34,

307 GB40, GB70) were grown and maintained at 37ºC in hypoxic conditions (3% O_2, 5% CO_2) in

308 NeuroCultTM NS-A Proliferation medium (STEMCELL Technologies, 05751) supplemented with

309 1% Heparin Solution (STEMCELL Technologies, 07980), 2% Amphotericin B (Fungizone,

310 EuroClone, ECM0009D), 10ng/mL bFGF (Sigma-Aldrich, FO291), 20ng/mL EGF (Sigma-

311   Aldrich, E9644), and 1% Penicillin/Streptomycin. Cells were passaged when 70-80% confluent,

312   and media were changed regularly.

Sample Preparation

314   Prior to preparation, U87 cells were detached with 10mM EDTA for 15min at 37°C. GBM cells

315   were mechanically detached or collected from suspension in growth media. Cells were pelleted,

316   counted, and resuspended to a concentration of 3×10^6 cells/mL. Polystyrene beads were added to

317   the cell suspensions in a 1:20 ratio (1×10^{10} stock solution, Life Technologies, FluoSpheres™

318   Polystyrene Microspheres, F1308), and incubated with gentle mixing for 30-45 min at 37°C.

319   Hyaluronic acid (HA) hydrogels were prepared concurrent with cell preparation. Frozen

320   lyophilized thiol-modified hyaluronan (Glycosil®, Advanced BioMatrix, GS222) and

321   polyethylene glycol diacrylate (Extralink-Lite®, Advanced BioMatrix, GS3008) were thawed and

322   dissolved with degassed deionized water to 50mg/mL and 5mg/mL, respectively, and vortexed for

323   45 min. For each sample, a volume of 40µL of cell-bead solution was added to 160µL Glycosil®

324   and mixed thoroughly with a micropipette. Immediately thereafter, 40µL Extralink-Lite® solution

325   was added and thoroughly mixed, such that the final concentration of the hyaluronan was

326   33.3mg/mL. For optical trap measurements, samples were prepared by pipetting 33µL solution

327   onto a glass microscope slide. A chamber was created by adding a coverslip to each side of the

328   slide and across the top, fixed with double-sided tape. For immunofluorescence imaging, the gel

329   solution was pipetted into plastic wells affixed to a microscope slide. The gels were allowed to

330   polymerize for 1 hr. at 37°C, after which cell growth media was added to hydrate the samples.

331   Polymerization continued overnight, and samples were measured or fixed at 24-28 h post

332   preparation.

Immunofluorescence Imaging

334   Samples were fixed in 4% PFA for 2 h at room temperature. Samples were washed 3 x 10 min

335   with PBS, and blocked and permeabilized for 1 h at room temperature in PBST (PBS containing

336   0.1% Tween 20) + 0.5% Triton X-100. Samples were washed 3 x 10min with PBS, then incubated

337   for 2 h at room temperature in a staining solution of PBST containing a 1:50 dilution of phalloidin

338   and 1:1000 dilution of Hoechst 33342. Samples were washed with PBS 3 x 10 min prior to

339   imaging. Samples were imaged on a Zeiss 780 laser scanning confocal microscope with Plan-

340   Apochromat 40x/1.4 NA Oil DC M27 objective. Presented images are maximum intensity

341   projections of 1μm z stacks.

Quantification of Circularity

343   Analysis was performed in FIJI using the built-in circularity plugin within the *Analyze Particles*

344   command. Maximum intensity projections of the phalloidin channel of single cells (GB40 n = 9;

345   GB70 n = 6) were thresholded and circularity was determined on a scale of 0-1 using the formula

346   *circularity = $4\pi(area/perimeter^2)$*. Differences between cell lines were determined using an

347   unpaired, two-tailed Student's *t* test.

Mass Spectrometry

349   GBM cells (GB40 and GB70) were seeded at concentrations of 250,000 per well in a 6 well plate

350   and starved for 24 hrs replacing conventional media with growth factor free media. Cells were

351   then washed twice with PBS 1X and lysed in 50 μL of Mammalian Protein Extraction lysis buffer

352   (Thermo Fisher Scientific) supplemented with phosphatase inhibitor cocktails 2 and 3 (Sigma

353   Aldrich) and protease inhibitor (Sigma Aldrich) at 1:100. After 1 hour of incubation on ice,

354   proteins were collected from supernatants after spinning down for 15 min at 12,000 x g. Collected

355   supernatants were stored in 1.5 mL tubes at -80 degrees Celsius.

356   The filter-aided sample preparation (FASP) protocol [49] was used with minor

357   modifications for the digestion of cell lysates. Briefly, lysates were reduced with 10mM DTT at

358   55°C for 30min, then diluted in a Microcon YM-10 filter unit with 8 M urea in 100mM Tris-HCl

359   (pH 8.5 [UA]) and centrifuged at 20°C for 30 minutes at 14,000 x g. Samples were washed with

360   200 µL UA, and protein was alkylated using 50mM in UA for 6 minutes at 25°C. This was followed

361   by centrifugation at 20°C for 30min at 14,000 x g, and excess reagent was removed. Samples were

362   washed with 3 x 100 µL of 8 M urea in 100 mM Tris-HCl (pH 8.0 [UB]), then diluted to 1 M urea

363   with 100 mM Tris-HCl (pH 8.0). Proteins were digested with trypsin at a ratio of 1:100 trypsin to

364   protein w/w overnight at 37°C. Recovery of tryptic peptides was performed by centrifugation at

365   20°C for 30 minutes at 14,000 x g, then washing the filter with 50 µL 0.5 M NaCl. Peptides were

366   desalted and acidified using a C18 SepPak cartridge (Waters, Milford, MA) and dried using

367   vacuum concentration (Labconco, Kansas City, MO). Dried peptides were fractionated by high pH

368   reversed-phase spin columns (Thermo Fisher Scientific), lyophilized, and solubilized in 4%

369   acetonitrile and 0.5% formic acid in water. Fractions were separated on a 75 µm x 15 cm, 2 µm

370   Acclaim™ PepMap™ reverse phase column (Thermo Fisher Scientific) with an UltiMate™ 3000

371   RSLCnano HPLC (Thermo Fisher Scientific) at a flow rate of 300 nL/min. Online analysis was

372   performed by tandem mass spectrometry using an Orbitrap Fusion™ mass spectrometer (Thermo

373   Fisher Scientific). Peptides were eluted into the spectrometer in linear gradients from 96% mobile

374   phase A (0.1% formic acid in water) to 35% mobile phase B (0.1% formic acid in acetonitrile)

375   over a period of 240 minutes. The Orbitrap mass analyzer was set to acquire data at 120,000

376   FWHM resolution, from which parent full-scan mass spectra were collected. Ions were isolated in

377   the quadrupole mass filter, then fragmented in the HCD cell (normalized energy 32%, stepped ±

378   3%). Product ions were then analyzed in the ion trap.

379 Mass spectrometry data and label-free quantification were performed using the MaxQuant

380 version 1.5.7.4 [50, 51]. Parameters were set as follows: variable modifications – methionine

381 oxidation and N-acetylation of protein N-terminus; static modification – cysteine

382 carbamidomethylation; first search performed using 20 ppm error; main search performed using

383 10 ppm error. Maximum of two missed cleavages; protein and peptide FDR threshold of 0.01; min

384 unique peptides 1; match between runs; label-free quantification with minimal ratio count 2. The

385 Uniprot human database from November 2016 (20,072 entries) was used to identify proteins, and

386 statistical analysis was performed using Perseus version 1.5.6.0 [52]. Contaminants, reversed

387 sequences, and proteins quantified in only one of three experimental replicates were removed.

388 Label-free quantification values were base 2 logarithmized, and missing values were imputed from

389 a normal distribution of the data. A two-way Student's t test was performed, with a p-value cutoff

390 of 0.05. Fold change was determined relative to global median base 2 logarithmic values across

391 all samples. The adjusted p value and negative logarithm of the adjusted p value were calculated

392 using the Holm-Sidak method with an alpha <0.05 in GraphPad Prism 8.0.2. Pathway enrichment

393 was performed using the Cytoscape version 3.7.2, wherein the top 150 most statistically significant

394 differentially regulated proteins were entered into the STRING Enrichment application. Output

395 was limited to Gene Ontology (GO) Function terms with an FDR <0.05. Pathways with at least

396 four proteins are plotted, with the exception of the parent terms "binding" and "protein binding"

397 which contained 112 and 73 proteins, respectively. Of these 150 proteins, the fifty most

398 differentially abundant proteins are plotted as a heatmap.

399 **Optical Trap Instrumentation and Setup**

400 *Instrumentation and Setup*. Our home-built setup was used as previously described [22, 24]. The

401 setup consists of a 1064 nm trapping beam (IPG Photonics, #YLR-20-1064-Y11) and a 975 nm

402   detection beam (Lumics, #LU0975M00-1002F10D) mounted on 5-axis adjustable mounts

403   (Newport, New Focus 9081).

404   The trapping beam is steered by a dual-axis acousto-optic deflector (AOD) (IntraAction,

405   DTD274HD6), which oscillates the trap at frequency ω. Before entering the AOD, the trapping

406   beam is linearly polarized by polarizing beam splitter cubes (Thorlabs, PBS23), and the beam is

407   attenuated manually by half-wave plates (Thorlabs, WPH05M-1064) or electronically via analog

408   output from a data acquisition (DAQ) card (National Instruments, PCIe-5871R FPGA). The AOD

409   receives control signals from radio frequency generating cards (Analog Devices, #AD9854/PCBZ)

410   with onboard temperature-controlled crystal oscillators (Anodyne Components, ZKG10A1N-

411   60.000M), and the cards are controlled by the DAQ card. After passing through the AOD, an iris

412   the doubly diffracted beam (i.e. 1st order in both transverse axes). To detect the displacement of

413   the trapping beam position, a beam sampler mirror (Thorlabs, BSF10-C) and neutral density (ND)

414   filter (Thorlabs, NENIR210B) direct a small amount of power (~1%) onto the trap-assigned

415   quadrant photodiode (QPD) (First Sensor, QP154-QHVSD). The trap beam is expanded by a lens

416   pair (Thorlabs, LA1509-C, 100mm; AC508-200-B, 200mm) and directed through a dichroic

417   mirror (Chroma, T1020LPXR).

418   The detection beam is expanded by a lens pair (Thorlabs, LA1131-C, 50mm; AC508-200-

419   b, 200mm) and directed through the dichroic mirror, where it is coupled into and collocated with

420   the trapping beam. A third telescopic lens pair (Thorlabs, LA113-C, 50mm; LA1384-CA, 125mm)

421   expands both beams, and a dichroic filter cube (Chroma, ZT1064rdc-2p) sends both beams into

422   the objective (Nikon, MRDO7602 CFIPLAN-APO VC60XA WI 1.2 NA), such that the trapping

423   beam slightly overfills the back aperture of the objective. A high numerical aperture (NA), long

424   working distance (WD) condenser (Nikon, WI 0.9 NA) collects light from the objective. A dichroic

425   mirror (Chroma ZT1064RDC-2P) directs the detection beam through a relay lens that is positioned

426   to image the back focal plane of the condenser onto the detection-assigned QPD. A bandpass filter

427   (Chroma, ET980/20X) removes the trapping beam from the path to the detection-assigned QPD.

428   Time-correlated 'trap' and 'detection' QPD signals are collected by analog inputs of the DAQ

429   card.

430   A charge-coupled device (CCD) camera is mounted on the optical table such that camera

431   position can be adjusted to a plane conjugate to the trapping beam AOD, back aperture of the

432   condenser, and detection QPD. The Hx-nm constant relating the AOD RF control signal (in Hz)

433   to the beam displacement (in nm) is calibrated by attenuating and focusing the beam on a coverslip

434   and imaging the backscattered beam on the CCD camera.

435   The alignment of the beams and the back focal plane interferometer is confirmed before

436   each experiment, and laser power is measured at the microscope backport with a power meter

437   (Fieldmate, Coherent) and adjusted to 100 mW at the half-wave plate. A flow chamber is

438   constructed from a microscope slide and coverslide with double-sided tape (Scotch) and loaded by

439   capillary action with polystyrene beads (Life Technologies, F1308) suspended in water. To ensure

440   proper alignment, a bead is trapped and the trap beam is oscillated while bead position is viewed

441   in real time from the detection QPD signal, and the beam-coupling dichroic and QPD position are

442   adjusted until oscillations in both transverse axes are centered on the QPD. A thermal power

443   spectrum is recorded and fitted to a Lorentzian function to calculate the viscosity of the water to

444   confirm system calibration. Before measurement, the camera pixel coordinates of the trap beam's

445   position are found by fitting a centroid to the intensity of an image collected of a trapped, stationary

446   bead in water.

447   *Sample Measurement.* The condenser is placed in Kohler illumination and the sample is placed in

448   focus. The bead of interest is positioned precisely in the center of the trap by scanning it through

449   the detection beam in three dimensions using a piezo XYZ nanopositioning stage (Prior,

450   #77011201) while voltages are recorded from the QPD. The characteristic V-nm relation, β, of

451   QPD voltage vs. position was calibrated in situ by fitting the central linear region of the detector

452   response to scanning the bead through the detection beam in the direction of the oscillations, giving

453   β in V-nm, as previously described [24]. Once the bead is correctly positioned, the trap beam is

454   oscillated while both trap and detection QPD signals are recorded. The oscillation is multiplexed

455   as a superposition of sine waves of differing phase and frequency, with the same amplitude (25.4

456   nm) at each frequency. Frequencies are prime numbers, in the range of 3Hz-15kHz, to avoid

457   interference. Four phases are interlaced to minimize the total amplitude of the composite

458   waveform. The waveform is pulsed for 2 s, followed by 2s with the trap stationary to obtain active

459   and passive spectra, respectively, and the sequence is repeated 7 times. Control and data collection

460   were conducted in custom programs (National Instruments, LabVIEW).

461   *Determination of Mechanical Properties*. The optical trap stiffness is determined *in situ* from the

462   active and passive power spectra using the active-passive calibration method [53, 54]. The linear

463   viscoelastic mechanical response of the material is modeled by a generalized Langevin equation

464   with additional force terms (a harmonic term accounting for the attractive potential of the optical

465   trap and an acceleration memory term accounting for the elastic in-phase response) [54-57].

466   Mechanical response for undriven motion is described as $m\ddot{x}_U(t) = F_{random}(t) - kx_U(t) - $

467     $\int_0^\infty \gamma_{1,U}(\tau)\dot{x}_U(t-\tau)d\tau - \int_0^\infty \gamma_{2,U}(\tau)\ddot{x}_U(t-\tau)d\tau$, where t is time, τ is correlation time, $x_U(t)$,

468     $\dot{x}_U(t)$, and $\ddot{x}_U(t)$ respectively the undriven bead position, velocity, and acceleration, $F_{random}(t)$ is the

469   Brownian force, k is the optical trap stiffness, m is the bead mass, and $\gamma_{1,U}(\tau)$ and $\gamma_{2,U}(\tau)$ are

470   respectively the real and imaginary parts of the undriven friction relaxation spectrum. Driven

471   motion is described similarly as $m x_D(t) = F_{random}(t) - k(x_D(t) - x_L(t)) - \int_0^\infty \gamma_{1,D}(\tau) x_D(t -$

472   $\tau) d\tau - \int_0^\infty \gamma_{2,D}(\tau) x_D(t - \tau) d\tau$, where $x_D(t)$, $x_D(t)$, and $x_D(t)$ respectively the undriven bead

473   position, velocity, and acceleration, $x_L(t)$ is the position of the optical trap, and $\gamma_{1,D}(\tau)$ and $\gamma_{2,D}(\tau)$

474   are respectively the real and imaginary parts of the driven friction relaxation spectrum. The

475   fluctuation dissipation theorem identifies the undriven and driven friction relaxation spectra such

476   that $\gamma_{1,U}(\tau) = \gamma_{1,D}(\tau)$ and $\gamma_{2,U}(\tau) = \gamma_{2,D}(\tau)$, according to Onsager's regression hypothesis.

477   The friction relaxation spectrum is related to the active power spectrum $R_L(\omega)$ by the

478   equation $\gamma D(\omega) + i\omega m = \frac{k}{i\omega}\left(\frac{1}{i\omega R_L(\omega)} + 1\right)$ with probe frequency of the driving oscillation ω in

479   rad•s^{-1}. The optical trap stiffness $k = \frac{Re\{R_L(\omega)\}}{P_u(\omega)}$ is determined from the real part of the active power

480   spectrum $R_L(\omega) = \frac{x_{dr}(\omega)}{-i\omega x_L(\omega)}$, with $x_L(\omega)$ and $x_{dr}(\omega)$ as the Fourier transforms of the time series of

481   the positions of the trapping laser and driven bead, respectively, recorded while the trap is

482   oscillating; and the passive power spectrum $P_U(\omega) = \langle |x_U(\omega)|^2 \rangle$, where $x_U(\omega)$ is the Fourier

483   transform of the time series of the undriven bead's thermally fluctuating position while the trap is

484   held stationary.

485   The generalized Stokes-Einstein relation yields the complex shear modulus as a function

486   of frequency, G*(ω), of each bead's surrounding microenvironment according to the equation

487   $G^*(\omega) = \frac{i\omega \gamma_D(\omega)}{6\pi a}$, with bead mass m, hydrodynamic radius a, and the friction relaxation spectrum

488   $\gamma_D(\omega)$. The complex modulus, $G^* = |G^*|^{(i\delta)} = G' + iG''$, has magnitude $|G^*| = (G'^2 + G''^2)^{1/2}$ and

489   loss tangent $tan(\delta) = {}^{G''}\!/_{G'}$ encoding rigidity and hysteresivity, respectively, such that G' represents

490   the storage modulus and G'' represents the loss modulus.

491   ***Data analysis and statistics***.   For each cell analyzed, 3-5 beads were measured at different

492   locations within the cell. Only cells exceeding ~30 µm from the coverslip were analyzed. A

493   minimum of 30 cells were analyzed per cell line. Data were analyzed using custom MATLAB and

494   GraphPad Prism programs. Because the modulus magnitudes $|G^*(\omega)|$, G', and G'' are log-normal

495   distributed within a single bead, we characterize their central tendency and dispersion,

496   respectively, by the maximum-likelihood estimate of the log-transformed mean $\mu =$

497     $exp\left[\frac{1}{n}\sum_{i=1}^{n}\ln(x_i) + \frac{1}{2}\left[\frac{1}{n-1}\sum_{j=1}^{n}\left|\ln(x_j) - \frac{1}{n}\sum_{i=1}^{n}\ln(x_i)\right|^2\right]\right]$ and   the   maximum-likelihood

498   estimate of the log-transformed variance $\sigma^2 = \mu^2\left[exp\left[\frac{1}{n-1}\sum_{j=1}^{n}\left|\ln(x_j) - \frac{1}{n}\sum_{i=1}^{n}\ln(x_i)\right|^2\right]\right]$. We

499   assume normal distribution of beads within each cell and cells within the cell population, and thus

500   characterize their central tendencies and dispersions respectively by arithmetic mean and variance.

501   Active microrheology data are presented as mean complex, storage, or loss moduli vs frequency

502   from 7 Hz to 15 kHz. The data are also presented as the log 2 transformed pair-wise normalization

503   of the complex modulus, averaged across frequencies (mean ± standard deviation). Data

504   normalized to the complex modulus were analyzed by two-way ANOVA with Tukey's honestly

505   significant difference post-test.

506   ***Power Law Fitting***. Power law fitting was performed as previously described [16]. Briefly, non-

507   linear regressions to fit the power law $|G^*(\omega)| = A(\omega)^b$ were performed on the mean value at each

508   frequency of $|G^*(\omega)|$ from high frequencies only (400 Hz – 15 kHz). Fits were performed in

509   MATLAB using the Curve Fitting Application, with nonlinear least-squares regression using the

510   Levenberg-Marquardt algorithm and robust weighting with the Least Absolute Residual

511   procedure. The power law exponent b is plotted for each individual cell, and b values among cell

512   lines were analyzed by one-way ANOVA with Tukey's multiple comparisons test.

513

514
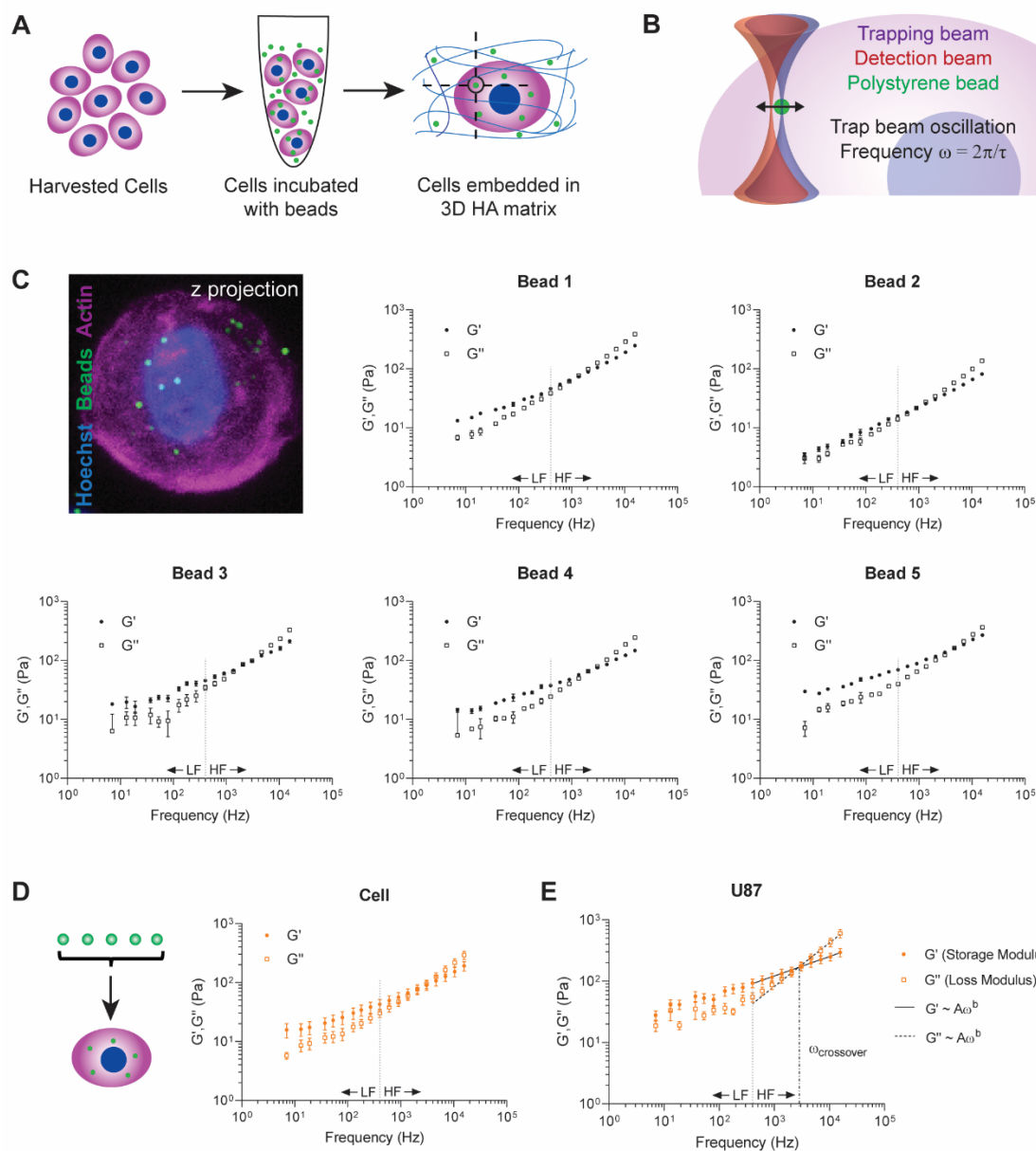
515 **Figure 1. Optical trap-based microrheology maps intracellular mechanic heterogeneity of**

516 **GBM cells in biomimetic model of brain ECM**

517 **A)** Schematic of experimental design. U87 cells were harvested and incubated with 1 μm

518 polystyrene beads in culture medium such that cells internalized the beads. Cells were then

519 embedded in hyaluronic acid hydrogels and incubated overnight. Measurements of individual

520 beads within cells were conducted 20-28h later. **B)** Schematic of optical trap measurement. Trap

521 beam oscillation frequencies ranged from 7Hz-15kHz, and each bead underwent 7 measurements

522 at each frequency. **C)** Micrograph of cell with internalized beads and G',G" values for 5 individual

523 beads in a single representative U87 cell (mean ± s.e., n ≤ 7 measurements). Micrograph staining

524 includes Hoechst (nucleus, blue), phalloidin (actin, magenta), and polystyrene beads (green). **D)**

525 Schematic and rheological values for a single cell (mean ± s.e., n = 5 beads). **E)** Average G',G"

526 values for U87 cell line (mean ± s.e., n = 30 cells). Low frequencies (LF) < 400 Hz. High

527 frequencies (HF) >400 Hz. HF values fit to power law G',G" ~ $A\omega^b$. For U87 cells, power law

528 coefficients A, exponents b, and 95% confidence intervals are as follows. U87 G': A = 13.71

529 (11.99, 15.43), b = 0.316 (0.3015, 0.3305); U87 G": A = 0.6091 (0.3175, 0.9007), b = 0.7095

530 (0.6573, 0.7617). The $\omega_{crossover}$ is the point at which the G' and G" power law curves intersect. For

531 U87 cells, $\omega_{crossover}$ = 2.73 kHz.

532

533

534

Figure 2. Patient-derived GBM cell lines show distinct rheological profiles.

A) Three primary GBM cell lines were derived from patients. The patient providing GB34 cells underwent standard resection and treatment, and the cells are derived from a biopsy of the recurring tumor. GB40 and GB70 cells are treatment-naïve. **B)** Average G', G" values for each primary GBM cell line (mean $\pm$ s.e., n $\geq$ 17 cells). Power law coefficients A, exponents b, and 95% confidence intervals are as follows. GB34 G': A = 21.23 (18.18, 24.28), b = 0.2675 (0.2508, 0.2843); GB40 G': A = 15.49 (12.73, 18.25), b = 0.2587 (0.2378, 0.2795); GB70 G': A = 34.87 (29.88, 39.87), b = 0.2308 (0.2139, 0.2477). GB34 G": A = 0.6455 (0.4317, 0.8593), b = 0.6879 (0.6517, 0.724); GB40 G": A = 0.5129 (0.3234, 0.7025), b = 0.6854 (0.645, 0.7257); GB70 G": A = 0.749 (0.4735, 1.024), b = 0.7116 (0.6715, 0.7517). The crossover frequencies for each line are as follows: GB34 $\omega_{crossover}$ = 4.06 kHz; GB40 $\omega_{crossover}$ = 2.94 kHz; GB70 $\omega_{crossover}$ = 2.95 kHz. **C)** The magnitude of the complex viscoelastic modulus $|G^*(\omega)|$ is plotted for primary and immortalized cell lines (mean $\pm$ s.e., n $\geq$ 17 cells). **D)** Pairwise log2 ratios of $|G^*(\omega)|$ across frequencies comparing all lines. Significance was determined using a 2-way ANOVA (* $p < 0.05$, ** $p < 0.01$, *** $p < 0.001$, **** $p < 0.0001$).

558

559
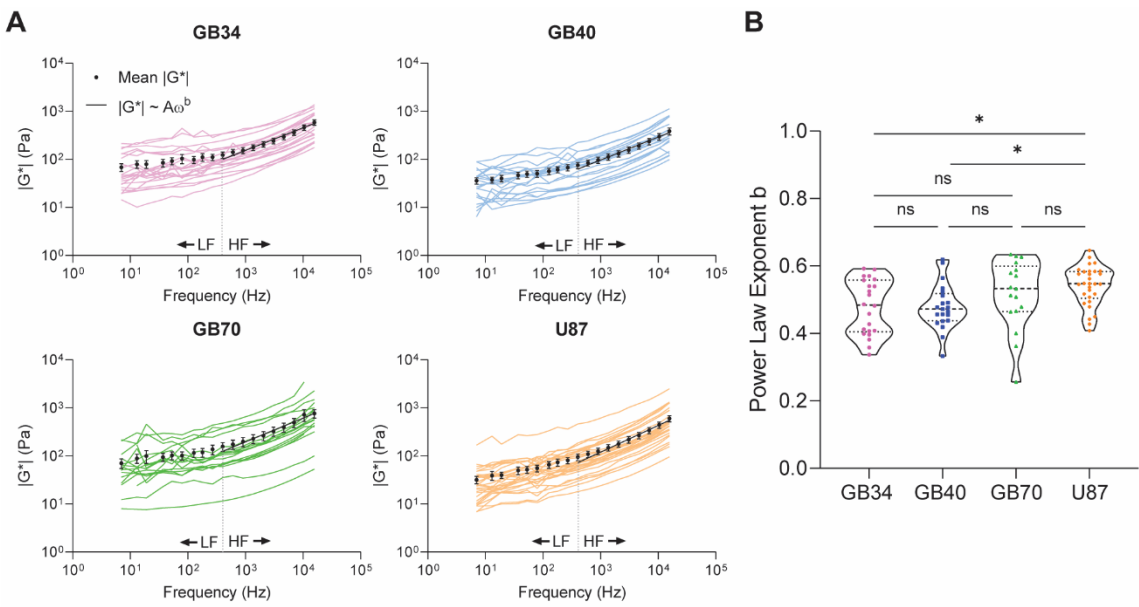
560 **Figure 3. Single cell analysis demonstrates line-specific power law-dependent rheological**

561 **profiles.**

562 **A)** Mean $|G^*(\omega)|$ values for each cell within its respective population accompanied by population

563 average (mean ± s.e.). HF population mean values were fit to the power law $G^* \sim A\omega^b$. The power

564 law coefficients A, exponents b, and 95% confidence intervals are as follows: GB34 $|G^*|$: A =

565 5.897 (3.142, 8.652), b = 0.471 (0.4186, 0.5234); GB40 $|G^*|$: A = 3.545 (1.927, 5.163), b =

566 0.4782 (0.4271, 0.5293); GB70 $|G^*|$: A = 6.431 (1.854, 11.01), b = 0.4947 (0.4152, 0.5742); U87

567 $|G^*|$: A = 2.593 (0.979, 4.206), b = 0.555 (0.4861, 0.624). **B)** The HF values of individual cells

568 were fit to the power law $G^* \sim A\omega^b$. The exponent b for each cell is displayed, along with median

569 and first and third quartiles for each line. Significance was determined using a one-way ANOVA

570 with Tukey's multiple comparisons test. (* adjusted p value < 0.05)

571

572

573

574

575

576
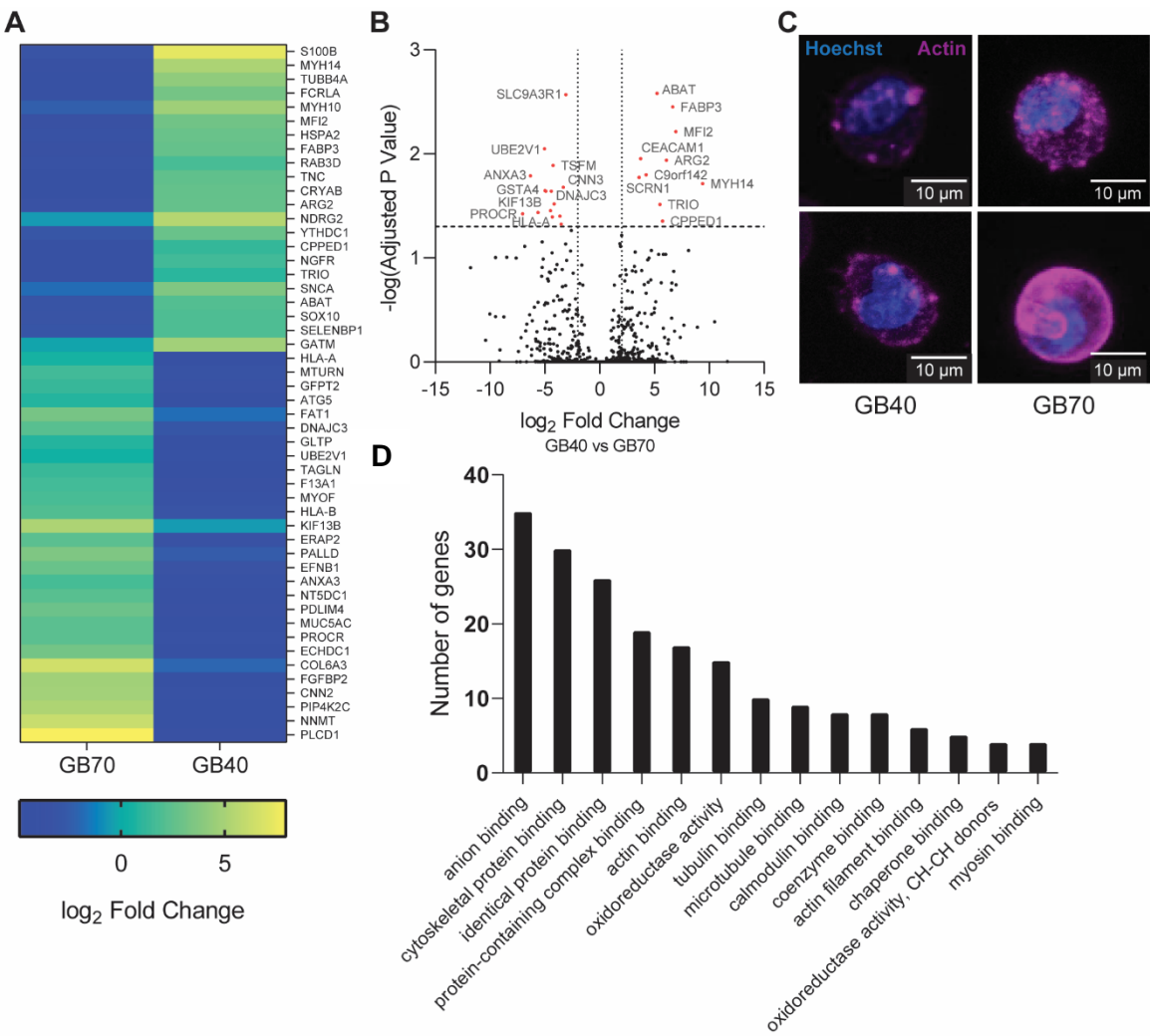
577   **Figure 4. Primary GBM lines show differential abundance of proteins associated with**

578   **cytoskeletal organization.**

579   **A)** Mass spectrometry analysis indicates differentially abundant proteins between GB40 and GB70

580   lines. Heatmap displays top 50 statistically significant (p < 0.05) most differentially abundant

581   proteins. Fold change was determined relative to the global median $\log_2$ values across all samples.

582   **B)** Volcano plot displaying $\log_2$ fold change vs the negative logarithm of the adjusted p value,

583   calculated using the Holm-Sidak method with $\alpha < 0.05$. Horizontal line indicates the negative log

584   of adjusted p value with $\alpha = 0.05$. Vertical lines indicate a $\log_2$ fold change of $\pm$ 2. **C)**

585   Representative micrographs of cells from GB40 and GB70 lines. Staining includes Hoechst

586   (nuclei, blue) and phalloidin (actin, magenta). **D)** Pathways enriched in the GB40 line compared

587   to the GB70 line among top 150 most statistically significant differentially abundant proteins.

588   Pathway analysis was limited to Gene Ontology (GO) Function terms with FDR < 0.05.

589

590
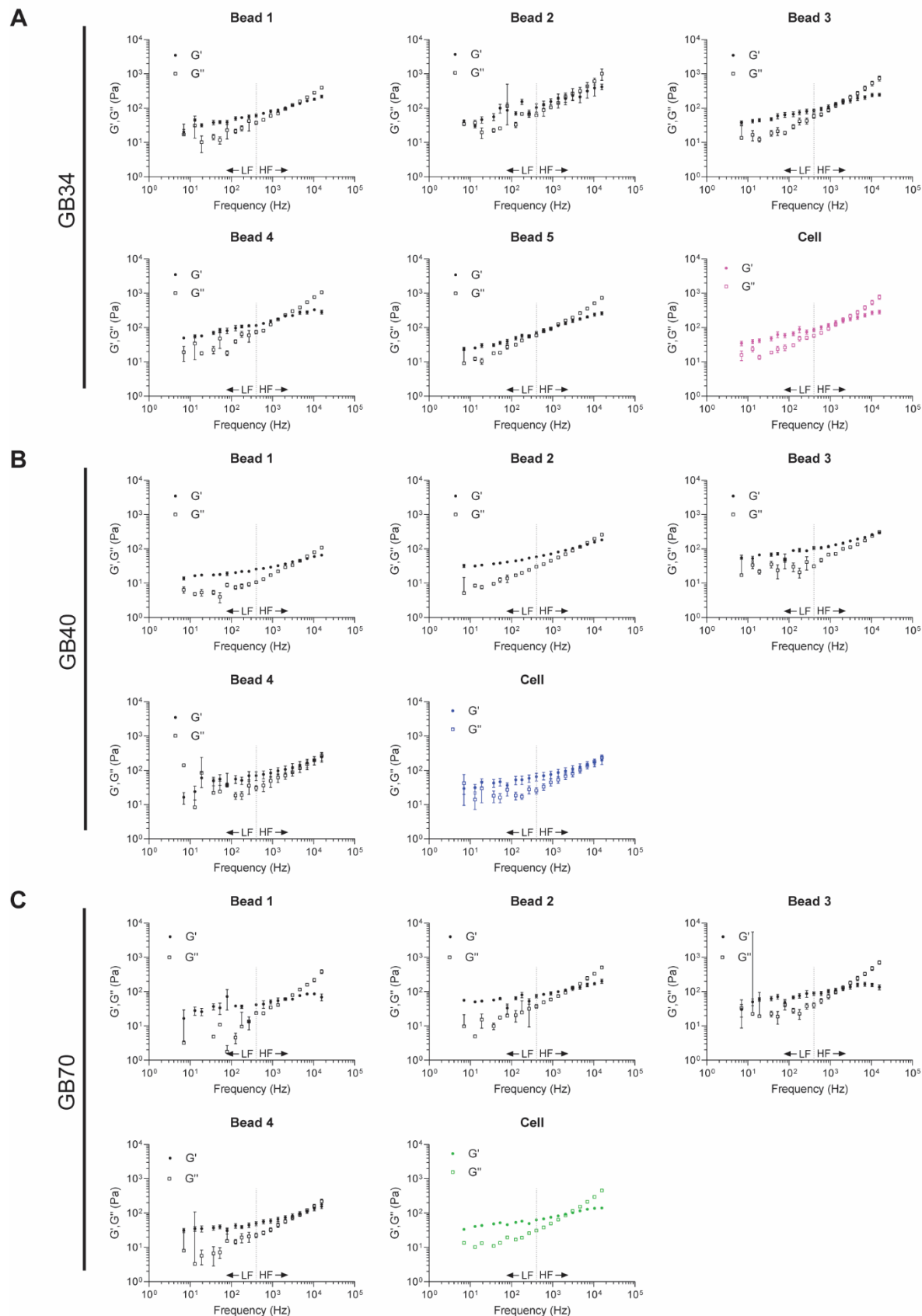
591 **Supplemental Figure 1. Intracellular mechanical heterogeneity in primary GBM cells.**

592 **A-C)** Rheological analysis of representative cells from lines GB34 (**A**), GB40 (**B**), and GB70 (**C**).

593 Bead values for G' and G'' are the average of individual measurements performed on the bead at

594 each frequency (mean $\pm$ s.e., $n \leq 7$), and cell values are the average (mean $\pm$ s.e.) of the beads

595 displayed. Low frequencies (LF) < 400 Hz. High frequencies (HF) >400 Hz.

596

597

598
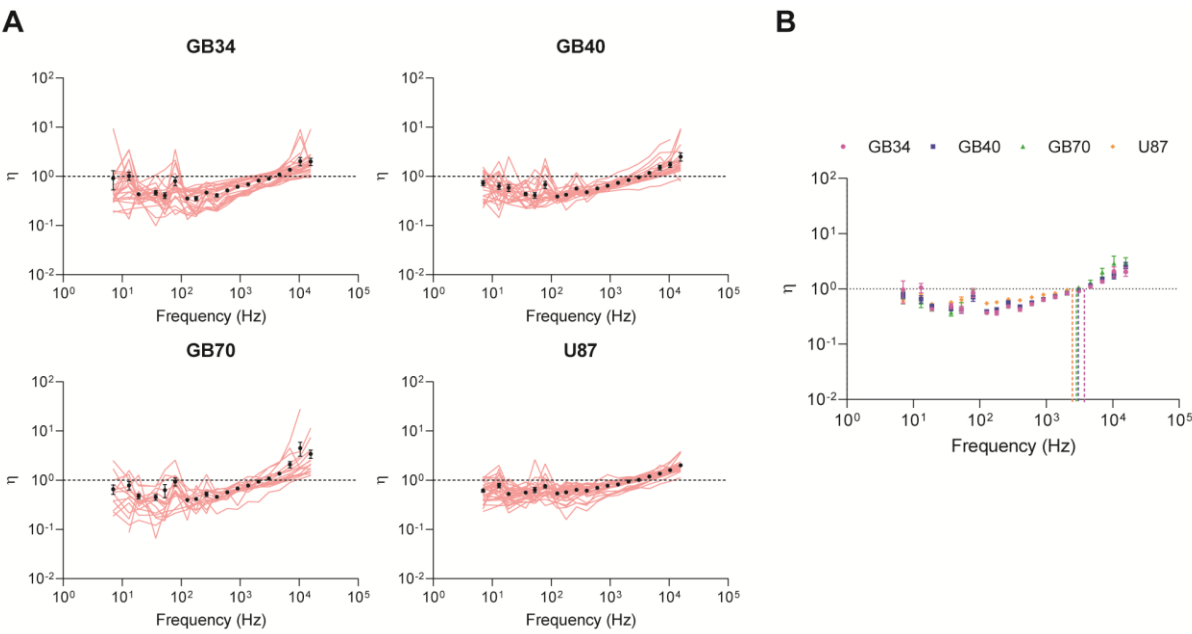
599 **Supplemental Figure 2. Single cell analysis of hysteresivity (η) among GBM lines.**

600 **A)** Mean $\eta(\omega)$ values for each cell within its population, accompanied by the respective population

601 average (mean ± s.e., n ≥ 17 cells). Semifluid materials are described with $\eta=1$, while $\eta=0$ for

602 purely elastic materials and η is infinite for purely viscous materials. **B)** Population averages for

603 each GBM line (mean ± s.e.). **C)** Pairwise log2 ratios of $\eta(\omega)$ across frequencies comparing all

604 lines. Significance was determined using a 2-way ANOVA (* $p < 0.05$, ** $p < 0.01$, *** $p < 0.001$,

605 **** $p < 0.0001$).

606

607

608
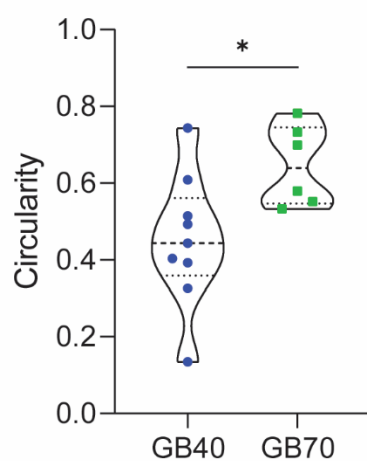
609   **Supplemental Figure 3. Single cell analysis indicates differences in circularity profiles among**

610   **primary GBM cell lines.**

611   Circularity measurements were performed on micrographs of cells with phalloidin staining of

612   actin. A circularity of 1 indicates a perfect sphere. Measurement was performed in FIJI with built-

613   in circularity plugin according to the formula $circularity = 4\pi(area/perimeter^2)$. Significance was

614   determined using an unpaired, two-tailed Student's t test (* $p < 0.05$).

615

References

616   References

617   1.   Aldape, K., et al., *Challenges to curing primary brain tumours.* Nat Rev Clin Oncol, 2019.
618   **16**(8): p. 509-520.
619   2.   Jacob, F., et al., *A Patient-Derived Glioblastoma Organoid Model and Biobank*
620   *Recapitulates Inter- and Intra-tumoral Heterogeneity.* Cell, 2020. **180**(1): p. 188-204 e22.
621   3.   Neftel, C., et al., *An Integrative Model of Cellular States, Plasticity, and Genetics for*
622   *Glioblastoma.* Cell, 2019. **178**(4): p. 835-849 e21.
623   4.   Barnes, J.M., L. Przybyla, and V.M. Weaver, *Tissue mechanics regulate brain*
624   *development, homeostasis and disease.* J Cell Sci, 2017. **130**(1): p. 71-82.
625   5.   Dumas, A.A., et al., *Microglia promote glioblastoma via mTOR-mediated*
626   *immunosuppression of the tumour microenvironment.* EMBO J, 2020: p. e103790.
627   6.   Gillespie, S. and M. Monje, *An active role for neurons in glioma progression: making*
628   *sense of Scherer's structures.* Neuro Oncol, 2018. **20**(10): p. 1292-1299.
629   7.   Pine, A.R., et al., *Tumor Microenvironment Is Critical for the Maintenance of Cellular*
630   *States Found in Primary Glioblastomas.* Cancer Discov, 2020. **10**(7): p. 964-979.
631   8.   Jackson, S., et al., *Model systems for studying the blood-brain barrier: Applications and*
632   *challenges.* Biomaterials, 2019. **214**: p. 119217.
633   9.   Tanner, K., *Perspective: The role of mechanobiology in the etiology of brain metastasis.*
634   APL Bioeng, 2018. **2**(3): p. 031801.
635   10.   Liu, C.J., et al., *Glioma Cell Migration Dynamics in Brain Tissue Assessed by Multimodal*
636   *Optical Imaging.* Biophys J, 2019. **117**(7): p. 1179-1188.
637   11.   Rezk, R., et al., *Spatial heterogeneity of cell-matrix adhesive forces predicts human*
638   *glioblastoma migration.* bioRxiv, 2020: p. 2020.05.06.080804.
639   12.   Nia, H.T., et al., *Solid stress and elastic energy as measures of tumour*
640   *mechanopathology.* Nature Biomedical Engineering, 2016. **1**(1): p. 0004.
641   13.   Pegoraro, A.F., P. Janmey, and D.A. Weitz, *Mechanical Properties of the Cytoskeleton*
642   *and Cells.* Cold Spring Harb Perspect Biol, 2017. **9**(11).
643   14.   Urbanska, M., et al., *Single-cell mechanical phenotype is an intrinsic marker of*
644   *reprogramming and differentiation along the mouse neural lineage.* Development, 2017.
645   **144**(23): p. 4313-4321.
646   15.   Wu, P.H., et al., *A comparison of methods to assess cell mechanical properties.* Nat
647   Methods, 2018. **15**(7): p. 491-498.
648   16.   Staunton, J.R., et al., *High-frequency microrheology in 3D reveals mismatch between*
649   *cytoskeletal and extracellular matrix mechanics.* Proc Natl Acad Sci U S A, 2019. **116**(29):
650   p. 14448-14455.
651   17.   Mathieu, S. and J.B. Manneville, *Intracellular mechanics: connecting rheology and*
652   *mechanotransduction.* Curr Opin Cell Biol, 2019. **56**: p. 34-44.
653   18.   Streitberger, K.-J., et al., *How tissue fluidity influences brain tumor progression.*
654   Proceedings of the National Academy of Sciences, 2020. **117**(1): p. 128-134.
655   19.   Streitberger, K.J., et al., *High-resolution mechanical imaging of glioblastoma by*
656   *multifrequency magnetic resonance elastography.* PLoS One, 2014. **9**(10): p. e110588.
657   20.   Bunevicius, A., et al., *REVIEW: MR elastography of brain tumors.* Neuroimage Clin, 2020.
658   **25**: p. 102109.

659   21.   Pepin, K.M., et al., *MR Elastography Analysis of Glioma Stiffness and IDH1-Mutation*
660   *Status.* AJNR Am J Neuroradiol, 2018. **39**(1): p. 31-36.
661   22.   Blehm, B.H., et al., *In vivo tissue has non-linear rheological behavior distinct from 3D*
662   *biomimetic hydrogels, as determined by AMOTIV microscopy.* Biomaterials, 2016. **83**: p.
663   66-78.
664   23.   Neuman, K.C. and S.M. Block, *Optical trapping.* Rev Sci Instrum, 2004. **75**(9): p. 2787-
665   809.
666   24.   Staunton, J.R., et al., *In situ calibration of position detection in an optical trap for active*
667   *microrheology in viscous materials.* Opt Express, 2017. **25**(3): p. 1746-1761.
668   25.   Trepat, X., G. Lenormand, and J.J. Fredberg, *Universality in cell mechanics.* Soft Matter,
669   2008. **4**(9): p. 1750-1759.
670   26.   Golomb, E., et al., *Identification and characterization of nonmuscle myosin II-C, a new*
671   *member of the myosin II family.* J Biol Chem, 2004. **279**(4): p. 2800-8.
672   27.   Wylie, S.R. and P.D. Chantler, *Myosin IIC: a third molecular motor driving neuronal*
673   *dynamics.* Mol Biol Cell, 2008. **19**(9): p. 3956-68.
674   28.   Stupp, R., et al., *High-grade glioma: ESMO Clinical Practice Guidelines for diagnosis,*
675   *treatment and follow-up.* Ann Oncol, 2014. **25 Suppl 3**: p. iii93-101.
676   29.   Bhaduri, A., et al., *Outer Radial Glia-like Cancer Stem Cells Contribute to Heterogeneity*
677   *of Glioblastoma.* Cell Stem Cell, 2020. **26**(1): p. 48-63 e6.
678   30.   Arbore, C., et al., *Probing force in living cells with optical tweezers: from single-molecule*
679   *mechanics to cell mechanotransduction.* Biophys Rev, 2019. **11**(5): p. 765-782.
680   31.   Antonacci, G., et al., *Recent progress and current opinions in Brillouin microscopy for life*
681   *science applications.* Biophys Rev, 2020. **12**(3): p. 615-624.
682   32.   Guck, J., et al., *The optical stretcher: a novel laser tool to micromanipulate cells.* Biophys
683   J, 2001. **81**(2): p. 767-84.
684   33.   Munder, M.C., et al., *A pH-driven transition of the cytoplasm from a fluid- to a solid-like*
685   *state promotes entry into dormancy.* Elife, 2016. **5**.
686   34.   Nikolic, M. and G. Scarcelli, *Long-term Brillouin imaging of live cells with reduced*
687   *absorption-mediated damage at 660 nm wavelength.* Biomed Opt Express, 2019. **10**(4):
688   p. 1567-1580.
689   35.   Lu, Y.B., et al., *Viscoelastic properties of individual glial cells and neurons in the CNS.*
690   Proc Natl Acad Sci U S A, 2006. **103**(47): p. 17759-64.
691   36.   Mandal, K., et al., *Mapping intracellular mechanics on micropatterned substrates.* Proc
692   Natl Acad Sci U S A, 2016. **113**(46): p. E7159-E7168.
693   37.   Balland, M., et al., *Power laws in microrheology experiments on living cells: Comparative*
694   *analysis and modeling.* Phys Rev E Stat Nonlin Soft Matter Phys, 2006. **74**(2 Pt 1): p.
695   021911.
696   38.   Fabry, B., et al., *Scaling the microrheology of living cells.* Phys Rev Lett, 2001. **87**(14): p.
697   148102.
698   39.   Kasza, K.E., et al., *The cell as a material.* Curr Opin Cell Biol, 2007. **19**(1): p. 101-7.
699   40.   Rigato, A., et al., *High-frequency microrheology reveals cytoskeleton dynamics in living*
700   *cells.* Nat Phys, 2017. **13**(8): p. 771-775.
701   41.   Broedersz, C.P. and F.C. MacKintosh, *Modeling semiflexible polymer networks.* Reviews
702   of Modern Physics, 2014. **86**(3): p. 995-1036.

703 42. de Sousa, J.S., et al., *Double power-law viscoelastic relaxation of living cells encodes*
704 *motility trends.* Sci Rep, 2020. **10**(1): p. 4749.
705 43. Ivkovic, S., et al., *Direct inhibition of myosin II effectively blocks glioma invasion in the*
706 *presence of multiple motogens.* Mol Biol Cell, 2012. **23**(4): p. 533-42.
707 44. Beadle, C., et al., *The role of myosin II in glioma invasion of the brain.* Mol Biol Cell, 2008.
708 **19**(8): p. 3357-68.
709 45. Picariello, H.S., et al., *Myosin IIA suppresses glioblastoma development in a mechanically*
710 *sensitive manner.* Proc Natl Acad Sci U S A, 2019. **116**(31): p. 15550-15559.
711 46. Lee, W., S. Lim, and Y. Kim, *The role of myosin II in glioma invasion: A mathematical*
712 *model.* PLoS One, 2017. **12**(2): p. e0171312.
713 47. Galli, R., et al., *Isolation and characterization of tumorigenic, stem-like neural precursors*
714 *from human glioblastoma.* Cancer Res, 2004. **64**(19): p. 7011-21.
715 48. Paul, C.D., et al., *Probing cellular response to topography in three dimensions.*
716 Biomaterials, 2019. **197**: p. 101-118.
717 49. Wisniewski, J.R., et al., *Universal sample preparation method for proteome analysis.* Nat
718 Methods, 2009. **6**(5): p. 359-62.
719 50. Cox, J., et al., *Accurate proteome-wide label-free quantification by delayed normalization*
720 *and maximal peptide ratio extraction, termed MaxLFQ.* Mol Cell Proteomics, 2014.
721 **13**(9): p. 2513-26.
722 51. Cox, J. and M. Mann, *MaxQuant enables high peptide identification rates, individualized*
723 *p.p.b.-range mass accuracies and proteome-wide protein quantification.* Nat Biotechnol,
724 2008. **26**(12): p. 1367-72.
725 52. Tyanova, S., et al., *The Perseus computational platform for comprehensive analysis of*
726 *(prote)omics data.* Nat Methods, 2016. **13**(9): p. 731-40.
727 53. Fischer, M., et al., *Active-passive calibration of optical tweezers in viscoelastic media.*
728 Review of Scientific Instruments, 2010. **81**(1): p. 015103.
729 54. Fischer, M.B.-S., K, *Calibration of trapping force and response function of optical*
730 *tweezers in viscoelastic media.* 2007. **9**(8).
731 55. Berg-Sørensen, K. and H. Flyvbjerg, *Power spectrum analysis for optical tweezers.*
732 Review of Scientific Instruments, 2004. **75**(3): p. 594-612.
733 56. Berg-Sørensen, K., et al., *Power spectrum analysis for optical tweezers. II: Laser*
734 *wavelength dependence of parasitic filtering, and how to achieve high bandwidth.*
735 Review of Scientific Instruments, 2006. **77**(6): p. 063106.
736 57. Tolić-Nørrelykke, S.F., et al., *Calibration of optical tweezers with positional detection in*
737 *the back focal plane.* Review of Scientific Instruments, 2006. **77**(10): p. 103101.
738